

Ultra-fast Digital DPC Yielding High Spatio-Temporal Resolution for Low-Dose Phase Characterisation

Julie Marie Bekkevold^{1,2,*}, Jonathan J. P. Peters^{1,2}, Ryo Ishikawa³, Naoya Shibata³, and Lewys Jones^{1,2}

¹*School of Physics, Trinity College Dublin, College Green, Dublin D02 PN40, Ireland*

²*Advanced Microscopy Laboratory, Centre for Research on Adaptive Nanostructures and Nanodevices (CRANN), Trinity College Dublin, Dublin D02 DA31, Ireland*

³*Institute of Engineering Innovation, University of Tokyo, Bunkyo, Tokyo 113-8656, Japan*

August 16, 2024

*Corresponding author: bekkevoj@tcd.ie

Abstract

In the scanning transmission electron microscope, both phase imaging of beam-sensitive materials and characterisation of a material’s functional properties using *in-situ* experiments are becoming more widely available. As the practicable scan speed of 4D-STEM detectors improves, so too does the temporal resolution achievable for both differential phase contrast (DPC) and ptychography. However, the read-out burden of pixelated detectors, and the size of the gigabyte to terabyte sized data sets, remain a challenge for both temporal resolution and their practical adoption. In this work, we combine ultra-fast scan coils and detector signal digitisation to show that a high-fidelity DPC phase reconstruction can be achieved from an annular segmented detector. Unlike conventional analog data phase reconstructions from digitised DPC-segment images yield reliable data, even at the fastest scan speeds. Finally, dose fractionation by fast scanning and multi-framing allows for post-process binning of frame streams to balance signal-to-noise ratio and temporal resolution for low-dose phase imaging for *in-situ* experiments.

1 Introduction

Scanning transmission electron microscopy (STEM) is a commonly used technique for the structural, functional and chemical characterisation of materials at very high spatial resolution. In recent decades, the traditional monolithic bright field (BF) and annular dark field (ADF) detectors have started to be superseded by other geometries of detectors enabling new imaging techniques. One of these is the development of high dynamic range cameras capable of capturing the entire two-dimensional (2D) convergent beam electron diffraction (CBED) pattern for every 2D scan point on the specimen. This results in a four-dimensional (4D) dataset, and the detectors are therefore aptly referred to as 4D-STEM or pixelated detectors. These 4D detectors are becoming increasingly popular for many different types of materials

characterisation with imaging methods that require position-sensitive detectors to elucidate the internal structure of the bright field disk and overlapping regions with scattered disks.

A higher pixelation of the detector allows for a finer sampling of the CBED patterns at each probe position. However, the greater the number of pixels, the higher the read-out overhead from the detector, and the slower the minimum sample-plane dwell time achievable. When using pixelated detectors the minimum dwell time, or the minimum fly-back time, are not limited by the scan coils and generators of the microscope but rather by the detector read-out. The necessity of these increased dwell times in 4D-STEM can then introduce unwanted image artefacts due to sample drift or environmental instability [1–3], and makes *in-situ* characterisation challenging.

Recent advances in ptychographic reconstruction

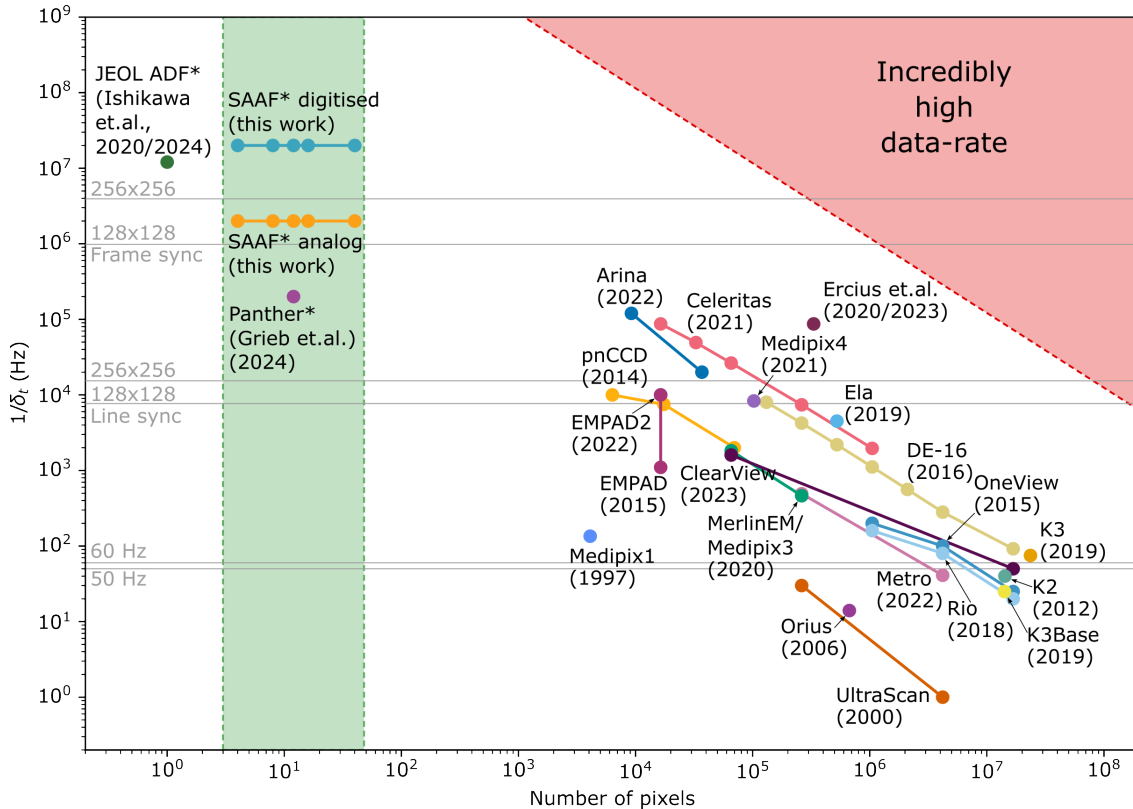


Figure 1: Illustration of the practicable scan speed (in $\frac{1}{\delta_t}$) versus number of segments/pixels for various commercially available or researched detectors. Several detectors may be operated in different binning modes, where higher binning allows for faster data readout due to lower pixel numbers. All the data for the 4D detectors has been acquired from data-sheets or publications reporting the highest practicable readout speed from the detectors [4–12]. For the detectors marked with * the scan speed is taken from publications and does not necessarily represent the highest possible speed achievable [3, 13]. Where several bit depth modes are available, the main reported readout speed is quoted (for details see Supplementary Information). Data used may be found at [14].

reaching information limits of less than 0.5 \AA uses both a high dwell time and high beam current which is challenging for samples that damage under beam irradiation [15]. The core assumption for ptychographic reconstruction that the sample is static poses challenges if the goal is to image dynamic processes *in-situ*. Especially when the minimum practicable dwell time for pixelated detectors is still typically found in the $10 - 1000 \text{ \mu s}$ regime. The assumption of the static object phase would only hold for samples that vary on time scales much higher than a few seconds, depending on the number of scan points (field of view) and the resolution required. Still, it should be mentioned that with iterative ptychography and defocused probes the dose delivered to the sample may be reduced and temporal resolution improved due to the increased sample-plane step size [16–18].

Since pixelated detectors were first used to acquire

images of the CBED in a STEM scan in the late 90's with the first Medipix-detector, the data rate has been increasing with the development of faster and higher pixel-number detectors; these include the TFS EMPAD (2015), Quantum Detectors MerlinEM (Medipix3, 2020), DirectElectron Celeritas (2021), and Dectris Arina (2022). To contextualise the speed and pixelation of various detectors, these parameters are plotted in Figure 1. Most pixelated detectors support hardware binning of pixels to get a higher read-out speed at the expense of a lower CBED sampling. This binning leads to a lower read-out delay and data set size, and facilitates higher real-space scan speeds and for this reason some detectors in Figure 1 are represented by multiple points. Further, the type and dynamic ranges of the commercially available 4D-STEM detectors in Figure 1 are summarised in Table S1 in the Supplementary Information. For several detec-

tors the frame-rate may be increased by choosing a lower bit depth, essentially sacrificing dynamic range for speed. Still, bit depth does not tell the full story of the dynamic range achievable by the detector since some detectors encode more information than intensity recorded in the pixel in their output, with the result that a higher dynamic range is supported. At the time of writing, in terms of frame-rate for fully pixelated 4D detectors, the state of the art is the Dectris Arina detector with a minimum real-space dwell time of 10 μ s. [19].

Notice how, beginning with the Medipix 1 launched in 1997, the community has generally moved towards higher numbers of pixels and increasing practicable scan speed, approaching the generation of multi-TB datasets in hours – if not minutes [2, 20]. For completeness, a ‘single element’ detector case of ADF STEM is shown in the upper-left of Figure 1. We use the term elements here as a general term that can mean either pixels or detection segments. Segmented detectors from 4 to 40 elements fall within the green highlighted region. There is then a ‘pixelation gap’ in the range from 40 to \sim 3000 elements which the authors imagine may be an active area of technology development in the coming years.

To avoid image distortions arising from power supply instability, it is often desirable to sync the start of each pixel, line or even frame to the power supply frequency [1]. In Figure 1, the horizontal lines labelled 50 and 60 Hz indicate the threshold of dwell time (camera frame rate) where syncing the start of each pixel to the power supply frequency is possible. For example, this shows that the Gatan UltraScan CCD, released around the year 2000, is not able to pixel-sync to A.C. mains frequency for 4D-STEM. Similarly, the horizontal lines labelled “Line sync” indicate the minimum frame speed (maximum dwell time) where syncing the start of each line to a 60 Hz mains frequency becomes possible, in a 128 by 128 or 256 by 256 pixel image respectively. Lastly, the “Frame sync” lines indicate the scan speed at which syncing the start of each frame to a 60 Hz mains frequency would be possible, again for 128 by 128 and 256 by 256 pixel images.

With the 4D nature of the data sets, the increasing number of pixels in the detectors, and the hardware’s ever-increasing scan speed, experiment data rate increases massively. We are now in the era where generating massive (multiple PB) data sets from single microscope sessions is no longer uncommon [2, 20]. The triangular area in the top right corner of Figure 1 corresponds roughly to the range where

Terabit per second data-rates (Tbps) would start to arise, but the question remains whether these massive data sets are truly necessary. From a sustainability perspective, these high data rates are problematic. Abiding by the FAIR data principles, requiring our data to be Findable, Accessible, Interoperable, and Reusable, demands that we store all our raw data in non-proprietary data formats, in an accessible way [21, 22]. Most research data is required to stay stored and available for at least a few years requiring on-site hard-drives or cloud storage space. This often means that cloud storage, and online repositories such as Zenodo [23], are the only viable options regardless of the carbon footprint of that. Electricity consumed by data centres currently accounts for 0.3 % of world carbon emissions, and storing 1TB of data in the cloud results in 2 tons of CO₂ emissions per year [24–26]. For comparison, this is about the same carbon footprint as a round-trip flight from Dublin to San Francisco [27].

While 4D-STEM enables high-resolution imaging in both the image and detector plane, there are also position-sensitive detectors with a lower number of discrete segments which have been shown to yield high-quality image data for phase contrast techniques such as ptychography, optimum bright field (OBF), and differential phase contrast (DPC). Specifically, DPC has long been established as a powerful tool for probing both magnetic and electric fields inside samples, including the local electric fields surrounding individual atoms [28–31]. Although reliable DPC signals depend on minimal dynamical scattering, and thus requires a very thin sample, there are several examples where the functional properties of specimens, such as ferroelectric domain formation or internal magnetic fields, have been characterised with fewer numbered segmented detectors [31–33]. Furthermore, a significant amount of noteworthy high-quality DPC imaging has been done with as low as four annular segments [3, 31, 34–37]. Similarly, almost a decade ago, Yang et. al. showed that for single-side-band (SSB) ptychography the signal-to-noise ratio (SNR) of the reconstructed image does not increase significantly with increased detector plane pixelation beyond around 16x16 [38]. And just a few years ago, Ooe et. al. demonstrated impressive low-dose phase reconstruction with the OBF technique with a 16 segmented annular detector [32].

For an annular, four-quadrant segmented detector, the minimum dwell time for precise scanning is no longer limited by the read-out from the detector but rather by the practicable scan speed of the STEM

itself. Once the readout overhead becomes negligible, the STEM scan may be done at very high speeds with dwell times far less than a microsecond. With high-speed scan coils and state-of-the-art scan controllers, dwell times as low as 50 ns are readily available [8, 37]. This low dwell time enables multi-frame imaging at speeds close to TV-rate, paving the way for phase contrast imaging with temporal resolution for *in-situ* experiments. However, at significantly reduced dwell times the temporal response of the detector becomes important. Several works have previously shown how scintillator-based detectors have a scintillation decay time which causes the duration of single electron events to last over 0.5 μs , sometimes as long as 1.5 μs [39–45]. When scanning at dwell times slower than around twice the scintillator decay time, the effects of this afterglow is negligible, but for faster scans, the image begins to suffer from streaking artefacts as a result of scintillator decay [39, 44]. A potential solution to this is to use low enough beam current to be able to count the individual electrons in the image, either in post-processing [42, 46], or by live in-hardware digitisation of the signal from the detector photo-multiplier tube (PMT) [45]. By digitising the signal from the detector in real-time, the streaking artefacts seen for analog images are removed and more information is retained in the fast scan direction.

In this work, we combine for the first time ultra-fast scan coils [8] and in-hardware digitisation of segmented scintillator-based detector [45] to show that digitisation allows for much faster usable frame-rates and paves the way for low-dose phase characterisation, with potential use cases in beam-sensitive and low atomic number materials, as well as *in-situ* experiments.

2 Low-dose approaches with DPC

For beam-sensitive materials that either change characteristics or damage under electron beam irradiation, the possibilities for reduced dose is vital for precise characterisation. Collection efficiency can be thought of as the fraction of electrons that passed through the sample which are then used to generate signal. Whereas HAADF typically detects up to about 10% of the primary beam’s electrons, an annular detector in the annular bright field (ABF) region may reach $\sim 80\%$ collection [47]. Similarly, positioning a four-segment DPC detector in the ABF region yields an equally high collection efficiency [48]. The high collection efficiency of detectors with an outer

collection angle close to the semi-convergence angle (α) allows for a significant reduction in the beam current used, and as such is excellent for imaging beam-sensitive materials.

The dose applied to the sample, in units of electrons per unit area, may be expressed as:

$$\text{Dose} = \frac{I \cdot C \cdot \delta_t}{(dx)^2} \quad (1)$$

where I is the beam current, C the Coulomb number, δ_t the dwell time, and dx the pixel width. Importantly, this only accounts for the exposure during the image capture, whereas the complete exposure also includes the sample exposure during beam flyback [49]. Still Equation 1 clearly illustrates that reducing both beam current and dwell time is important to reach ultra-low dose conditions. When the δ_t reduction is limited for example for 4D-STEM imaging, the dose must be reduced by means of reducing the beam current or increasing the pixel width, since lowering the dwell time is not available. Finally, dose fractionation by multi-frame imaging has been shown to significantly reduce beam damage to the sample [50, 51]. Therefore, detectors with low enough read-out overhead to acquire many frames at a high enough frame rate for the sample to remain unchanged during a single frame capture also benefits beam sensitive samples.

The phase shift imposed on the electron beam by the sample causes redistribution of the beam in the diffraction plane, which may be detected as a net displacement of the center-of-mass (COM) of the CBED pattern. This COM displacement is proportional to the gradient of the phase shift acquired by the beam which, in the absence of magnetic fields in the specimen, is proportional to the electric field of the sample [29, 52]. With segmented detectors the COM in x-direction in detector space is estimated by:

$$\text{COM}_x(\vec{r}) = \sum_i I_i(\vec{r}) \cdot \vec{k}_{x_i} \quad (2)$$

where \vec{r} is the position in real space, \vec{k}_{x_i} is x-position of the center-of-mass of the i th detector segment [36]. The expression for COM_y follows similarly. For a four-segmented detector these calculations simplify to subtracting opposing detector segments in x- and y-directions. The vector signal $\mathbf{COM}(\vec{r})$ is proportional to the projected electric field of the sample. It then follows from Gauss’ law and the Poisson equation that the integrated signal, $i\text{COM}(\vec{r})$, is proportional to the projected electric potential of the sam-

ple [53]. This signal is typically calculated by integration in Fourier space,

$$\mathcal{F}\{\text{iCOM}(\vec{r})\}(\vec{k}) = \frac{\mathcal{F}\{\text{COM}(\vec{r})\}(\vec{k}) \cdot \vec{k}}{2\pi i k^2} \quad (3)$$

where \vec{k} is the position vector in reciprocal space [53]. We can therefore use this to retrieve the projected electric potential of our samples from the $\text{COM}(\vec{r})$ signal obtained from Equation 2.

3 Optimising detector geometry for low-dose iCOM

To investigate the fidelity of the COM signal and the reconstructed iCOM images from both segmented and pixelated detectors (with differing numbers of segments or pixels), a 4D dataset of a thin SrTiO_3 (STO) sample of 11.7 nm (30 unit cells) thickness with 50 frozen phonon configurations was simulated using abTEM [54]. To match the experimental data presented later, a 300 keV beam energy and a 30 mrad semi-convergence angle were used. The full 4D-STEM simulation (191x191 pixels) has a max collection angle of 60 mrad (2α). Different detector geometries (masks) were applied to the diffraction patterns and the resulting COM and iCOM images calculated using the python-based 4D-STEM data-handling software py4DSTEM [55]. To facilitate comparison with Yang et. al. [38] a finite dose of $6241 \text{ e}/\text{\AA}^2$ ($10 \text{ C}/\text{cm}^2$) was applied representing Poisson statistical uncertainty. A direct comparison of the resulting COM and iCOM images for eight different geometry detectors can be seen in Figure 2. The segmented annular detectors, 4 and 16, with four and sixteen segments respectively show a slight four-fold symmetry in the reconstructed images due to the four-fold symmetry of the detectors [38, 56, 57]. This four-foldedness is eliminated for the pixelated arrays, even at the coarse pixelation of 4x4 pixels.

The peak signal-to-noise ratio (PSNR) captures the ratio between the maximum possible power of a signal and the signal-disturbing noise. It is given as:

$$\text{PSNR} = 10 \log_{10} \left(\frac{\text{MAX}_i^2}{\text{MSE}} \right) \quad (4)$$

where MAX_i is the maximum image value range in the infinite dose image and the MSE is the mean squared error between the infinite and finite dose images [38]. Since we have both the full-field, infinite dose simulation and finite dose simulations we can

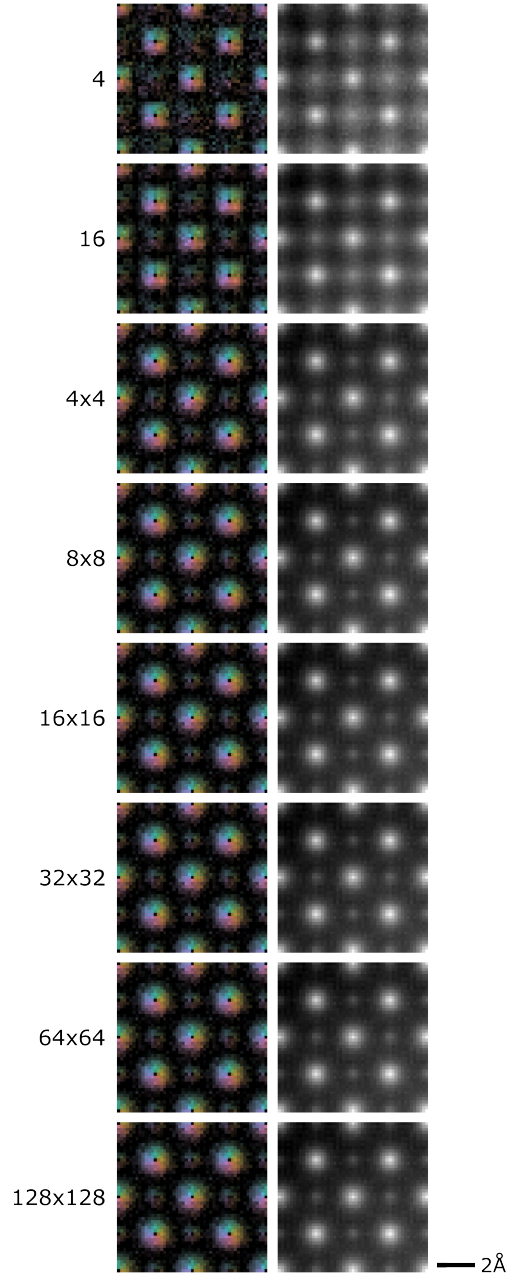


Figure 2: Finite dose ($6241 \text{ e}/\text{\AA}^2$) COM and iCOM images calculated from different virtual detector geometries.

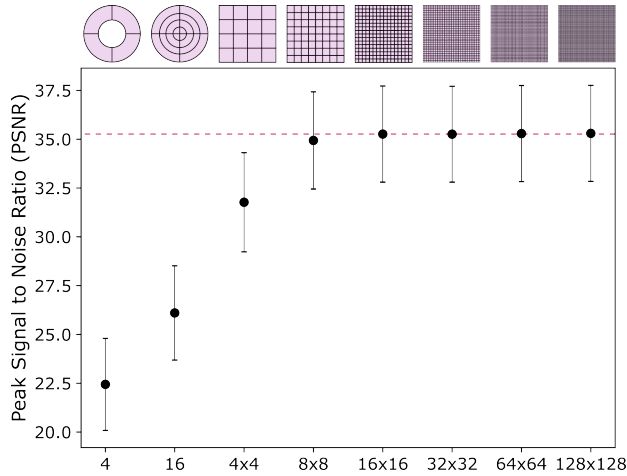


Figure 3: Peak signal-to-noise ratio in iCOM reconstructions from virtual detectors for a simulation of atomic resolution STO with 50 frozen phonon configurations and a finite dose of $6241 e/\text{\AA}^2$. The 4 denotes an annular detector with four segments and the 16 an annular detector with four rings of four segments each. Further, the rest denote pixelated array detectors. The dashed line is at the PSNR of the 16x16 pixel detector, highlighting that even the 8x8 pixel detector performs just barely worse than the higher number pixel detectors. The error bars are estimated from the statistical error arising from the MSE between the infinite and finite dose images.

define the PSNR as:

$$\text{PSNR} = 10 \log_{10} \left(\frac{\max(ref)^2}{(ref - expt)^2} \right). \quad (5)$$

Here, *ref* is the infinite dose reference image and *expt* is the finite dose image [38]. Figure 3 shows that the PSNR of the images in Figure 2 reaches a plateau once the detector pixelation is 16x16 pixels. This calculation was repeated for several different finite doses, calculating both iCOM and magnitude of COM signals, and they all show the same result of minimal improvement of the PSNR for higher number of pixels in the detector beyond 16x16 (see Supplementary Information). Since the improvement of iCOM phase retrieval is minimal for higher sampling of the CBED, the detector pixel count can be kept low to allow for faster scanning. This is not to say that larger format cameras are not useful, in fact they are used widely for strain mapping [58], PACBED [59, 60], crystallography characterisation with scanning electron (precession) diffraction (S(P)ED) [61–63], and more exotic applications like multi-beam electron diffraction [64] and patterned probe Bragg measurements [65]. Rather, it is just that for their use in

DPC and iCOM, the additional pixelation offers no advantage. Still, regardless of whether a pixelated or segmented detector is used, DPC places strong limitations on the experimental parameters like sample thickness, bending and the microscope operator’s ability to align the beam to zone axis. Because dynamical scattering and zone axis changes can produce a DPC signal indistinguishable from the DPC signal expected from an electric or magnetic field, careful considerations must be given to both sample preparation and the setup of the experiment [66, 67].

4D-STEM detection affords the opportunity to detect all the electrons from $0 - \alpha_{max}$, where α_{max} is the outer collection angle set by the camera length, often at high resolution. While this offers very precise estimates for the COM signal, there are several other works that suggest losing the center of the CBED, as we do when using an annular segmented detector, causes minor loss to the final iCOM signal [31, 36, 68–71]. A similar result has been shown for ptychography [72]. It has previously been shown that the PSNR of single side-band (SSB) ptychographic reconstruction of an isolated carbon atom increases very modestly for higher detector pixelation than 16x16 pixels [38]. Even segmented annular detectors of 4 and 16 segments can provide comparable ptychographic reconstructions. This further demonstrates how increasing pixelation of the detector is not necessarily better for phase contrast imaging. We may therefore reap the benefits of fewer element detectors (be they segments or pixels), to enable fast scanning and multi-frame to image with high spatial and temporal resolution. It should however be mentioned that low-dose ptychography is achievable and routinely performed using iterative ptychographic reconstruction algorithms [16–18, 73, 74]. These experiments often use highly defocused probes allowing large sample step sizes, which also improves the achievable temporal resolution. Additionally, more advanced methods like multi-slice ptychography and tilt-corrected BF-STEM are becoming more and more popular and showing promising results [75–78]. For such techniques, increased pixelation of the detector beyond 16x16 is advantageous.

4 Experimental digitisation

Using a probe-corrected JEOL Grand ARM operated at 300kV, single crystals of [100] oriented SrTiO₃ were imaged with a 5.2 pA beam current. Several fast dwell times in the range 50 ns to 1 μ s were collected with both with analog and digital signal recording. The

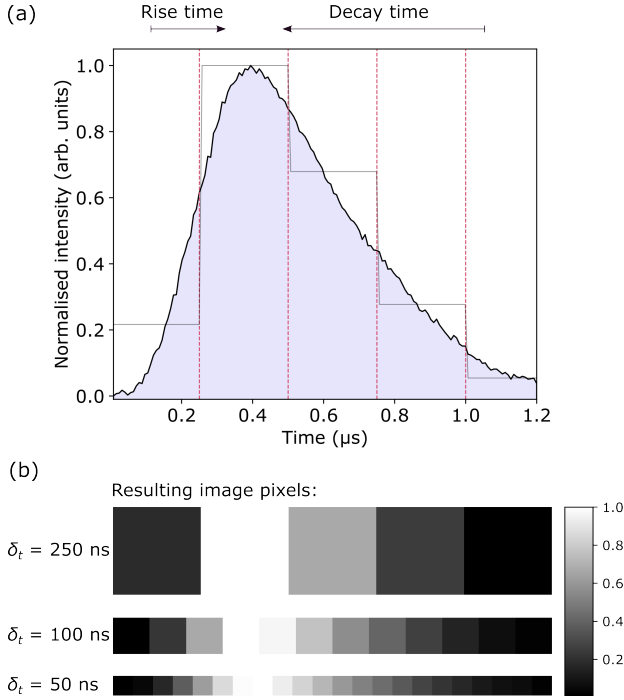


Figure 4: Single pulse from the SAAF detector with the 10-90% rise time and 90-10% decay time indicated. The vertical, dotted lines are the pixel boundaries for a 250 ns dwell time, and the stepped gray line indicates the normalised pixel intensity for each pixel with this dwell time. The (normalised) resulting image pixels are shown in the diagram below, for dwell times $\delta_t = 250, 100, 50$ ns respectively.

microscope used is equipped with fast low-inductance scan coils allowing dwell times as short as 50 ns to be reached [8]. For the DPC imaging we used a segmented annular all-field (SAAF) detector, which has 16 segments spread over four concentric rings with four segments each [34]. Performing the in-hardware digitisation has to be done on a per-segment basis and thus one channel per segment must be provided. For the experiments presented here, a four channel Pulse digitiser produced by turboTEM was used and the second ring from the center was chosen for the DPC imaging (see Supplementary Information). Digitisation of 8, 12, or 16 channels is possible by using additional Pulse digitisers in parallel so long as the scan unit can record their outputs (in this case a Gatan Digiscan 3 accepting four simultaneous channels was used). The outer collection angle of the detector annulus used was 32 mrad and the inner collection angle 16 mrad, for an $\alpha = 30$ mrad beam. A Pulse digitiser is easily retrofittable to any STEM system with

BNC cables, and the main demand is that the scan generator accepts the number of channels desirable – preferably directly as digital inputs. Both analog and digitised signals may be recorded simultaneously by forking the signal physically with a T-piece, provided that the number of input channels is sufficient. In order to facilitate multiple, parallel signal digitisation and multi-frame imaging, both analog and digital signal inputs are beneficial as well as a frame clock to aid multi-framing. A screenshot of the software for controlling the Pulse digitiser can be seen in the Supplementary Information.

Scintillator-based detectors have been shown to have quite significant electron detection event decay time, causing streaking artefacts in the images [40–42, 44]. A single electron event on the SAAF detector can be seen in Figure 4(a), with dotted lines indicating pixel boundaries for a dwell time of 250 ns. The full duration of the event is a combination of the time it takes for the scintillator to respond to the electron impact, the PMT to amplify the resulting light signal, and the read-out through the cables to the recording hardware. Additionally, scintillators often suffer from after-glow, meaning that they keep scintillating slightly for an extended time after exposure – even when the electron exposure is removed [43]. When the duration of any single electron event exceeds the pixel dwell time, the electron which was physically incident at the detector at a specific moment leads to signal intensity also for the following pixels. This causes streaking in the images, which may be seen in Figure 4(b), and as a result information about the sample is degraded in the fast scan direction [39, 44]. A consequence of the event duration of over a microsecond on this detector is that dwell times lower than that should be avoided to ensure the information integrity in the analog images. However, if the electron events are digitised using hardware for live PMT signal digitisation, lower dwell times become viable again [45].

The in-hardware digitisation calculates the gradient of the PMT signal and thresholds this to count the electron events. This results in a digitised signal which has a true zero noise floor, and where each electron is detected in the correct pixel only and all have the same intensity of unity. Digitising the signal from scintillator detectors has previously been demonstrated to significantly improve signal to noise ratio in HAADF images [43, 45]. Since the digitised pulse appears in the correct temporal position in the PMT stream it also appears in the correct spatial position in the image, without affecting subsequent

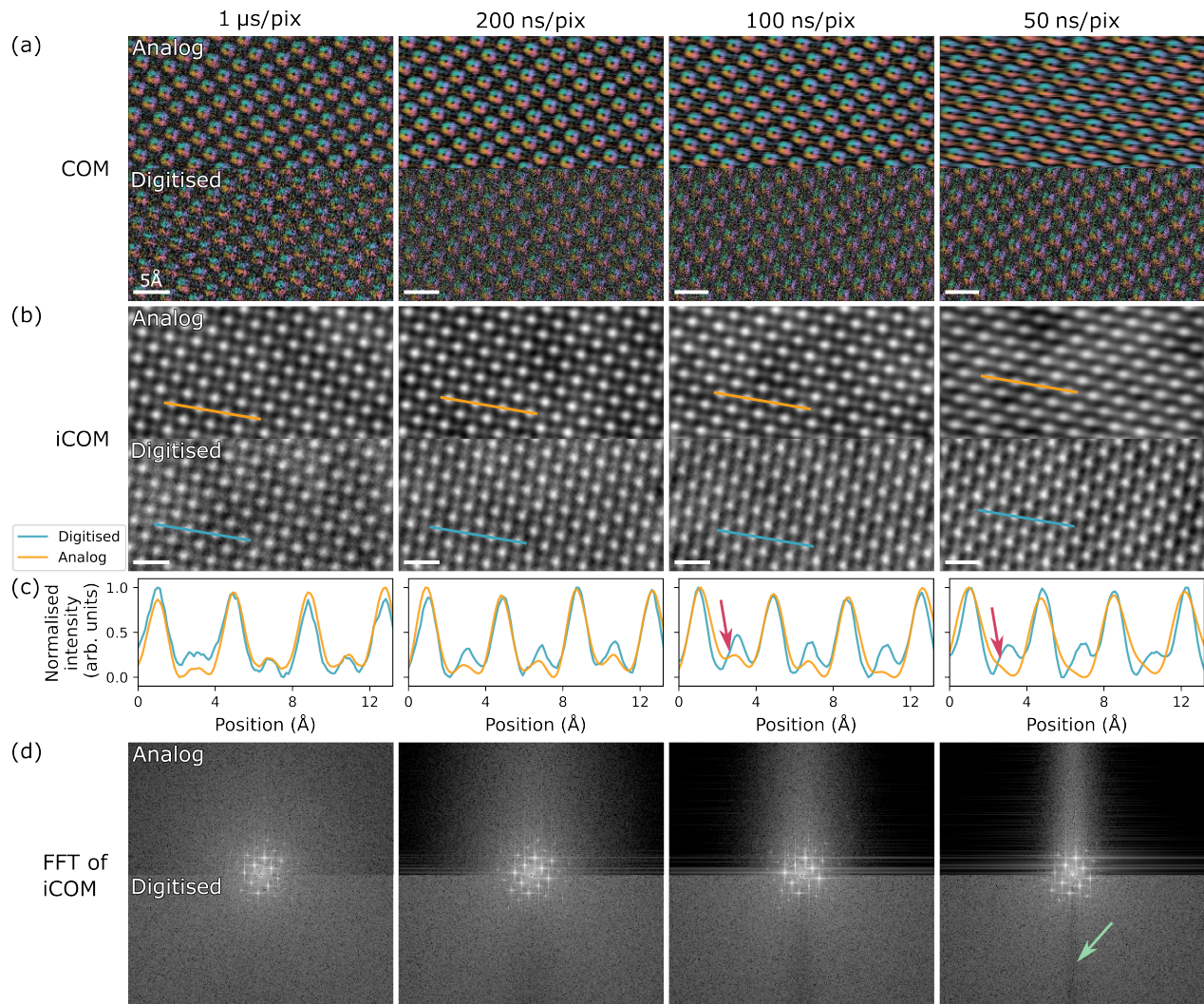


Figure 5: (a,b) Experimental COM and iCOM images, analog (top) and digitised (bottom), of STO acquired with beam current $I = 5.2$ pA and increasingly (left to right) lowered dwell times. The resolution in the analog images is severely reduced in the fast scan (horizontal) direction due to image streaking. (c) Line profiles from the lines indicated in (b), showing how the oxygen columns become increasingly unresolvable with analog DPC at the fastest scan speeds. (d) FFTs of iCOM images in (b) show how information is lost in the fast scan direction due to streaking.

pixels. As a result, all streaking artefacts are removed. Incidentally, there is some unavoidable few nanoseconds progressing time required by the digitisation hardware, but this manifests as a uniform apparent translation of the sample to the right by some constant fraction of a pixel width. Since scintillator detector surfaces are typically inhomogeneous, the electrons may be detected at different intensity depending on where on the detector surface they hit [41, 79]. Consequently, digitisation of the analog signal ensures a more homogeneous detector response, and yields an image that is quantitative, in number of

electrons [44, 79]. This ensures that detector inhomogeneity does not affect the COM calculations, and that denoising algorithms developed for quantised signals [80] may be used on the individual segment images before computing the COMs (although no denoising was used in this study). As a final advantage, having digitised signals makes quantitative comparison with simulations easier.

Figure 5 shows how streaking artefacts severely reduce information transfer in the fast scan direction for the analog images. The subtraction of one weak signal from another can be intrinsically noisy. In

DPC, subtracting opposing detector segment signals can also lead to the digital COM images appearing very noisy. This differs from the analog detector response which intrinsically performs a form of low pass filtering, yielding visually less noisy images. However, it is important to note that although the smoother images may be more visually appealing, this smoothing is the result of spatial resolution loss. By contrast, the iCOM reconstruction from the digitised signals show a very minimal information degradation, even at the fastest scan speed similar to the results for digital ADF imaging [43, 45]. Where the streaking cause the oxygen columns to be lost in the faster scan analog iCOM images, see line profiles in Figure 5, the digitised iCOM retain these columns very clearly. Notice especially how the background of the fast Fourier transforms (FFTs) are much flatter for the digitised iCOM images as compared with the analog iCOM images. This indicates that the information transfer is also much more isotropically reliable when digitising the PMT signal, and thus that the digitised iCOM images are more isotropically reliable.

For a STEM detector spanning the ADF region, a highly scattering point on the specimen will increase the arrival rate of electrons to the detector. Such mass-thickness type contrast often follows a Z^n relationship where n is around 1.7 depending on collection angle. Weakly scattering materials on the other hand are often studied with DPC due to the higher sensitivity for lower atomic numbers. Placing the DPC detector in the ADF region necessarily increases the arrival rate of electrons, relative to ADF, since the collection angles are within the semi-convergence angle. Although this aids collection efficiency, like all discrete counting processes, the arrival of two events approximately simultaneously may cause coincidence losses; a risk which increases dramatically at high beam currents. Using a significantly lowered beam current is then a convenient solution both to the need to avoid sample beam-damage, and avoid coincidence loss. Since coincidence loss is a process between adjoining detection events in *time* and not in space, these are only a factor along the fast-scan direction (and not between successive scan lines). This manifests in the Fourier transform (FT) as the formation of a dark band aligned perpendicular to the fast-scan direction. Since the fast-scan direction is presented horizontally by convention, this dark band runs vertically through the FT (see arrow in Figure 5(d)). The appearance of the faint vertical dark line in the FFT of the digital iCOMs suggests that at this beam current ($I = 5.2$ pA) some electron events are lost to

coincidence loss. In the slower scans the vertical dark band becomes broader since the coincidence loss persists at the same temporal domain but this becomes a higher spatial frequency in the image domain. By simulation, we have determined that the minimum separation for digitisation of two consecutive electron events for this specific detector is 259 ± 26 ns (for details see Supplementary Information). Importantly, this depends heavily on the beam current and the temporal response of the detector. For the beam current and detector used here this translates to loss of just under one electron per pixel for $\delta_t = 250$ ns, and approximately one every five pixels for $\delta_t = 50$ ns.

5 Time-resolution in multi-frame series

Reducing the beam current and using very low dwell times reduces the signal recorded in a single frame acquisition. In extreme cases, the image may contain so little signal that features are no longer distinguishable and phase reconstruction may fail. A useful signal level may be regained by scanning, drift correcting, and stacking many subsequent frames [50, 81]. In this way, the sample exposure to the beam is spread out over multiple passes of shorter exposures, reducing sample damage and enhancing signal integrity [82]. As would be expected, the PSNR increases with increasing number of summed frames as shown in Figure 6. As an example, achieving a time resolution of 4 seconds per output frame (at 512x512 image pixels) may be realised using 20 individual digital-DPC scan frames, each with $\delta_t = 50$ ns. Doing so yields an image with a PSNR of 16 without any denoising applied.

The iCOM phase reconstruction generally suffers from low-frequency artefacts, which are commonly filtered out using a high-pass filter [83, 84]. Applying a high-pass filter to the images in Figure 6 increases the PSNR by removing the low-frequency artefacts that arise from the phase reconstruction. This was achieved by subtracting a Gaussian filtered ($\sigma = 10$) version of the image. For consistency, the same high-pass filter was used for all images (see Supplementary Information for the difference images). That means that, depending on the necessary PSNR for the desired information to be extracted, time resolution of a few seconds may be realised with multi-frame, digital DPC imaging. Compared to 4D-STEM-based methods, where dwell times must typically be larger than 100 μ s and the time to acquire a single frame often

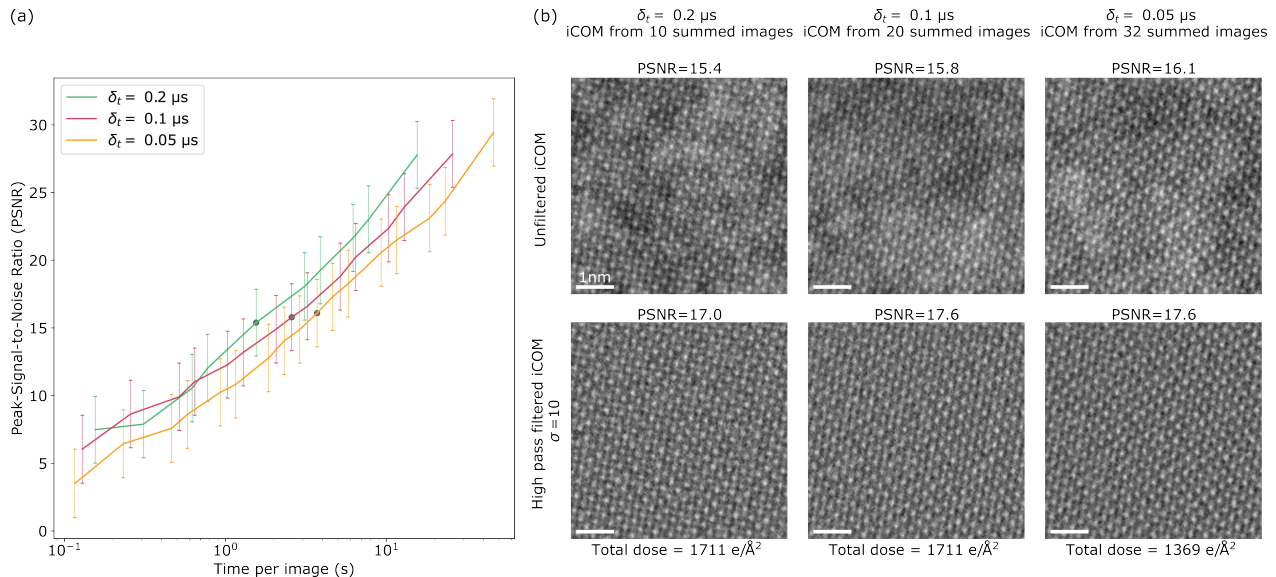


Figure 6: PSNR in iCOM images for various summing of multi-frame stacks. Time per image is then given as the combined time it took to acquire all the frames, e.g. for 20 summed frames the time per image is $20 \cdot T_{\text{Frame}}$. The images on the right are the result of summing 10, 20 and 32 frames respectively for the three different dwell times $\delta_t = 0.2, 0.1, 0.05 \mu\text{s}$. The top images are raw summed images and the bottom images are high-pass filtered.

reaches a few minutes, or sacrifice sampling or field-of-view, this is a huge improvement.

In the graph in Figure 6a we can see how the PSNR increases with increasing "time per image", which indicates that the more frames are summed the higher the PSNR in the final analysable image. It is also evident that for a given "time per image", the PSNR is generally higher if the frames are captured with a slower dwell time. While this might seem somewhat discouraging for adopting faster scan speeds, a major factor in this is the fly-back time. The faster the scan, the more frames are required to get enough signal for an analysable image, and the more times the beam must fly back. As a result, the time lost to line and frame fly-back is more significant for the faster scan and the temporal resolution achievable from the multi-frame stack may be worsened. In summary, it is vital in these experiments to balance the need for low beam current for viable digitisation, fast scanning for dose fractionation and temporal resolution, and fly-back time considerations. As a final note, with faster scintillators the practicable beam current is increased and with lower-hysteresis scan coils or fly-back compensation [49] the temporal resolution may be increased. Both of which, although beyond the scope of this work, may in the future increase the fidelity and practicability of digitised DPC and improve the temporal resolution for *in-situ* phase char-

acterisation.

6 Conclusions

Due to camera read-out overhead, the relatively slow dwell times required for 4D-STEM can introduce unacceptable image artefacts arising from sample drift or environmental instability. Additionally, the many-GB datasets generated by 4D-STEM cameras may be cumbersome to acquire, store and process. Scintillator-based segmented detectors exhibit negligible read-out overhead and far smaller dataset sizes, but where analog read-out speeds approach the scintillator decay-time other unacceptable artefacts arise. Smearing of the atomic columns in space, due to signal streaking in time, make the precise characterisation of subtle atomic column displacements virtually impossible. The demand for increased dwell times in both these cases stands in the way of ultra low-dose phase contrast imaging.

In this work, by in-hardware digitisation of the signal from a scintillator-based segmented detector, we have for the first time demonstrated phase imaging at massively improved speeds using a dwell time of 50 ns. We show that the digitised images, acquired at a relatively low beam current ($I = 5.2 \text{ pA}$) suffer minimally from coincidence loss, even with the detector under the direct forward beam. Multi-frame

bursts of ultra-fast acquired COM images are used to delay sample damage, accumulate sufficient signal for high-quality iCOM phase reconstruction, and retain temporal resolution for future *in-situ* studies in the STEM.

Acknowledgements

The authors would like to acknowledge the Advanced Microscopy Laboratory (AML) at the Centre for Research on Adaptive Nanostructures and Nanodevices (CRANN) and the Advanced Materials and BioEngineering Research (AMBER) Network for financial and infrastructural support for this work. JMB and JJJP acknowledge SFI grant number 19/FFP/6813, RI and NS acknowledge JST FOREST (Grant No. JPMJFR2033), JST ERATO (Grant No. JPMJER2202), and JSPS KAKENHI (Grant No. JP19H05788, 20H05659, JP22H04960, JP24H00373), and LJ acknowledges Royal Society and SFI grant number URF/RI/191637 and 12/RC/2278.P2.

Declaration of Interests

LJ is the creator of the SmartAlign image registration software used here and made available commercially by HREM Research (Tokyo). LJ and JJPP are co-founders and equity holders of turboTEM Ltd. (Dublin) who manufacture the ‘Pulse’ hardware signal digitiser used in this work.

References

- [1] Lewys Jones and Peter D. Nellist. “Identifying and Correcting Scan Noise and Drift in the Scanning Transmission Electron Microscope”. In: *Microscopy and Microanalysis* 19.4 (2013), pp. 1050–1060. DOI: 10.1017/S1431927613001402.
- [2] Colum M. O’Leary et al. “Increasing Spatial Fidelity and SNR of 4D-STEM Using Multi-Frame Data Fusion”. In: *Microscopy and Microanalysis* 28.4 (2022), pp. 1417–1427. DOI: 10.1017/S1431927621012587.
- [3] Tim Grieb et al. “GaN atomic electric fields from a segmented STEM detector: Experiment and simulation”. In: *Journal of Microscopy* (2024). DOI: 10.1111/jmi.13276.
- [4] G. Bardelloni et al. “A new read-out system for an imaging pixel detector”. In: *2000 IEEE Nuclear Science Symposium. Conference Record (Cat. No.00CH37149)*. 2000 IEEE Nuclear Science Symposium. Conference Record (Cat. No.00CH37149). Vol. 2. 2000, 12/57–12/60 vol.2. DOI: 10.1109/NSSMIC.2000.949940.
- [5] C Ponchut et al. “MAXIPIX, a fast readout photon-counting X-ray area detector for synchrotron applications”. In: *Journal of Instrumentation* 6.1 (2011), pp. C01069–C01069. DOI: 10.1088/1748-0221/6/01/C01069.
- [6] R. Ballabriga et al. “Medipix3: A 64 k pixel detector readout chip working in single photon counting mode with improved spectrometric performance”. In: *Nuclear Instruments and Methods in Physics Research Section A: Accelerators, Spectrometers, Detectors and Associated Equipment*. 11th International Workshop on Radiation Imaging Detectors (IWORID) 633 (2011), S15–S18. DOI: 10.1016/j.nima.2010.06.108.
- [7] Mark W Tate et al. “High Dynamic Range Pixel Array Detector for Scanning Transmission Electron Microscopy”. In: *Microscopy and Microanalysis* 22.1 (2016), pp. 237–249. DOI: 10.1017/S1431927615015664.
- [8] Ryo Ishikawa et al. “High spatiotemporal-resolution imaging in the scanning transmission electron microscope”. In: *Microscopy* 69.4 (2020), pp. 240–247. DOI: 10.1093/jmicro/dfaa017.
- [9] R. Ballabriga, M. Campbell, and X. Llopart. “An introduction to the Medipix family ASICs”. In: *Radiation Measurements* 136 (2020), p. 106271. DOI: 10.1016/j.radmeas.2020.106271.
- [10] Fulin Wang et al. “Electron backscattered diffraction using a new monolithic direct detector: High resolution and fast acquisition”. In: *Ultramicroscopy* 220 (2021), p. 113160. DOI: 10.1016/j.ultramic.2020.113160.
- [11] Hugh T. Philipp et al. “Very-High Dynamic Range, 10,000 Frames/Second Pixel Array Detector for Electron Microscopy”. In: *Microscopy and Microanalysis: The Official Journal of Microscopy Society of America, Microbeam Analysis Society, Microscopical Society of Canada* (2022), pp. 1–16. DOI: 10.1017/S1431927622000174.
- [12] Peter Ercius et al. *The 4D Camera: an 87 kHz direct electron detector for scanning/transmission electron microscopy*. 2023. DOI: 10.48550/arXiv.2305.11961.
- [13] Ryo Ishikawa et al. “Real-time tracking of three-dimensional atomic dynamics of Pt trimer on TiO₂ (110)”. In: *Science Advances* 10.9 (2024), eadk6501. DOI: 10.1126/sciadv.adk6501.
- [14] Julie Marie Bekkevold and Lewys Jones. *STEM detectors frame rates*. 2024. DOI: 10.5281/zenodo.11165245.
- [15] Kayla X. Nguyen et al. “Achieving sub-0.5-angstrom-resolution ptychography in an uncorrected electron microscope”. In: *Science* 383.6685 (2024), pp. 865–870. DOI: 10.1126/science.ad12029.
- [16] J. M. Rodenburg and H. M. L. Faulkner. “A phase retrieval algorithm for shifting illumination”. In: *Applied Physics Letters* 85.20 (2004), pp. 4795–4797. DOI: 10.1063/1.1823034.
- [17] Andrew M. Maiden and John M. Rodenburg. “An improved ptychographical phase retrieval algorithm for diffractive imaging”. In: *Ultramicroscopy* 109.10 (2009), pp. 1256–1262. DOI: 10.1016/j.ultramic.2009.05.012.

- [18] Liqi Zhou et al. “Low-dose phase retrieval of biological specimens using cryo-electron ptychography”. In: *Nature Communications* 11.1 (2020). Publisher: Nature Publishing Group, p. 2773. DOI: 10.1038/s41467-020-16391-6.
- [19] Daniel G Stroppa et al. “From STEM to 4D STEM: Ultrafast Diffraction Mapping with a Hybrid-Pixel Detector”. In: *Microscopy Today* 31.2 (2023), pp. 10–14. DOI: 10.1093/mictod/qaad005.
- [20] Steven R. Spurgeon et al. “Towards data-driven next-generation transmission electron microscopy”. In: *Nature Materials* 20.3 (2021), pp. 274–279. DOI: 10.1038/s41563-020-00833-z.
- [21] Mark D. Wilkinson et al. “The FAIR Guiding Principles for scientific data management and stewardship”. In: *Scientific Data* 3.1 (2016), p. 160018. DOI: 10.1038/sdata.2016.18.
- [22] Michelle Barker et al. “Introducing the FAIR Principles for research software”. In: *Scientific Data* 9.1 (2022), p. 622. DOI: 10.1038/s41597-022-01710-x.
- [23] European Organization For Nuclear Research and OpenAIRE. *Zenodo*. en. 2013. DOI: 10.25495/7GXK-RD71.
- [24] Christopher L. Weber, Jonathan G. Koomey, and H. Scott Matthews. “The Energy and Climate Change Implications of Different Music Delivery Methods”. In: *Journal of Industrial Ecology* 14.5 (2010), pp. 754–769. DOI: 10.1111/j.1530-9290.2010.00269.x.
- [25] Nicola Jones. “How to stop data centres from gobbling up the world’s electricity”. In: *Nature* 561.7722 (2018), pp. 163–166. DOI: 10.1038/d41586-018-06610-y.
- [26] Steven Gonzalez Monserrate. “The Cloud Is Material: On the Environmental Impacts of Computation and Data Storage”. In: *MIT Case Studies in Social and Ethical Responsibilities of Computing* (Winter 2022 2022). DOI: 10.21428/2c646de5.031d4553.
- [27] Joachim Ciers, Aleksandra Mandic, Laszlo Daniel Toth, and Giel Op ’t Veld. “Carbon Footprint of Academic Air Travel: A Case Study in Switzerland”. In: *Sustainability* 11.1 (2019). Number: 1 Publisher: Multidisciplinary Digital Publishing Institute, p. 80. DOI: 10.3390/su11010080.
- [28] H. Rose. “Phase-Contrast in Scanning-Transmission Electron-Microscopy”. In: *Optik* 39.4 (1974), pp. 416–436.
- [29] N. H. Dekkers and H. De Lang. “Differential phase contrast in a STEM”. In: *Optik* 41.4 (1974), pp. 452–456.
- [30] M. Lohr et al. “Differential phase contrast 2.0—Opening new “fields” for an established technique”. In: *Ultramicroscopy* 117 (2012), pp. 7–14. DOI: 10.1016/j.ultramicro.2012.03.020.
- [31] N. Shibata et al. “Differential phase-contrast microscopy at atomic resolution”. In: *Nature Physics* 8.8 (2012), pp. 611–615. DOI: 10.1038/nphys2337.
- [32] Kousuke Ooe, Takehito Seki, Yuichi Ikuhara, and Naoya Shibata. “Ultra-high contrast STEM imaging for segmented/pixelated detectors by maximizing the signal-to-noise ratio”. In: *Ultramicroscopy* 220 (2021), p. 113133. DOI: 10.1016/j.ultramicro.2020.113133.
- [33] Qiaoli Chen et al. “Imaging Beam-Sensitive Materials by Electron Microscopy”. In: *Advanced Materials* 32.16 (2020), p. 1907619. DOI: 10.1002/adma.201907619.
- [34] Naoya Shibata et al. “New area detector for atomic-resolution scanning transmission electron microscopy”. In: *Journal of Electron Microscopy* 59.6 (2010), pp. 473–479. DOI: 10.1093/jmicro/dfq014.
- [35] R. Close, Z. Chen, N. Shibata, and S.D. Findlay. “Towards quantitative, atomic-resolution reconstruction of the electrostatic potential via differential phase contrast using electrons”. In: *Ultramicroscopy* 159 (2015), pp. 124–137. DOI: 10.1016/j.ultramicro.2015.09.002.
- [36] Naoya Shibata et al. “Electric field imaging of single atoms”. In: *Nature Communications* 8.1 (2017), p. 15631. DOI: 10.1038/ncomms15631.
- [37] Ryo Ishikawa et al. “Spatial and phase resolution in electron microscopy”. In: *Microscopy* 72.2 (2023), pp. 78–96. DOI: 10.1093/jmicro/dfac045.
- [38] Hao Yang, Timothy J. Pennycook, and Peter D. Nellist. “Efficient phase contrast imaging in STEM using a pixelated detector. Part II: Optimisation of imaging conditions”. In: *Ultramicroscopy* 151 (2015), pp. 232–239. DOI: 10.1016/j.ultramicro.2014.10.013.
- [39] J. P. Buban et al. “High-resolution low-dose scanning transmission electron microscopy”. In: *Journal of Electron Microscopy* 59.2 (2010), pp. 103–112. DOI: 10.1093/jmicro/dfp052.
- [40] Florian F. Krause et al. “Effects of instrument imperfections on quantitative scanning transmission electron microscopy”. In: *Ultramicroscopy* 161 (2016), pp. 146–160. DOI: 10.1016/j.ultramicro.2015.10.026.
- [41] X. Sang and J. M. LeBeau. “Characterizing the response of a scintillator-based detector to single electrons”. In: *Ultramicroscopy* 161 (2016), pp. 3–9. DOI: 10.1016/j.ultramicro.2015.11.008.
- [42] Andreas Mittelberger, Christian Kramberger, and Jan-nik C. Meyer. “Software electron counting for low-dose scanning transmission electron microscopy”. In: *Ultramicroscopy* 188 (2018), pp. 1–7. DOI: 10.1016/j.ultramicro.2018.02.005.
- [43] Tiarnan Mullarkey, Clive Downing, and Lewys Jones. “Development of a Practicable Digital Pulse Read-Out for Dark-Field STEM”. In: *Microscopy and Microanalysis* 27.1 (2021), pp. 99–108. DOI: 10.1017/S1431927620024721.
- [44] Tiarnan Mullarkey et al. “How Fast is Your Detector? The Effect of Temporal Response on Image Quality”. In: *Microscopy and Microanalysis* 29.4 (2023), pp. 1402–1408. DOI: 10.1093/micmic/ozad061.
- [45] Jonathan J. P. Peters et al. “Electron counting detectors in scanning transmission electron microscopy via hardware signal processing”. In: *Nature Communications* 14.1 (2023), p. 5184. DOI: 10.1038/s41467-023-40875-w.
- [46] Ryo Ishikawa, Andrew R. Lupini, Scott D. Findlay, and Stephen J. Pennycook. “Quantitative Annular Dark Field Electron Microscopy Using Single Electron Signals”. In: *Microscopy and Microanalysis* 20.1 (2014), pp. 99–110. DOI: 10.1017/S1431927613013664.

- [47] Dmitri O. Klenov and Susanne Stemmer. “Contributions to the contrast in experimental high-angle annular dark-field images”. In: *Ultramicroscopy* 106.10 (2006), pp. 889–901. DOI: 10.1016/j.ultramic.2006.03.007.
- [48] Zhiyao Liang, Dongsheng Song, and Binghui Ge. “Optimizing experimental parameters of integrated differential phase contrast (iDPC) for atomic resolution imaging”. In: *Ultramicroscopy* 246 (2023), p. 113686. DOI: 10.1016/j.ultramic.2023.113686.
- [49] Tiarnan Mullarkey, Jonathan J. P. Peters, Clive Downing, and Lewys Jones. “Using Your Beam Efficiently: Reducing Electron Dose in the STEM via Flyback Compensation”. In: *Microscopy and Microanalysis* (2022), pp. 1–9. DOI: 10.1017/S1431927621013908.
- [50] Lewys Jones et al. “Smart Align—a new tool for robust non-rigid registration of scanning microscope data”. In: *Advanced Structural and Chemical Imaging* 1.1 (2015), p. 8. DOI: 10.1186/s40679-015-0008-4.
- [51] Lewys Jones et al. “Managing dose-, damage- and data-rates in multi-frame spectrum-imaging”. In: *Microscopy* 67 (suppl.1 2018), pp. i98–i113. DOI: 10.1093/jmicro/dfx125.
- [52] H. Rose. “Nonstandard Imaging Methods in Electron Microscopy”. In: *Ultramicroscopy* 2 (1977), pp. 251–267.
- [53] Ivan Lazić, Eric G.T. Bosch, and Sorin Lazar. “Phase contrast STEM for thin samples: Integrated differential phase contrast”. In: *Ultramicroscopy* 160 (2016), pp. 265–280. DOI: 10.1016/j.ultramic.2015.10.011.
- [54] Jacob Madsen and Toma Susi. “The abTEM code: transmission electron microscopy from first principles”. In: *Open Research Europe* 1.24 (2021). DOI: 10.12688/openreseurope.13015.2.
- [55] Benjamin H. Savitzky et al. “py4DSTEM: A Software Package for Four-Dimensional Scanning Transmission Electron Microscopy Data Analysis”. In: *Microscopy and Microanalysis* 27.4 (2021), pp. 712–743. DOI: 10.1017/S1431927621000477.
- [56] Daniel Joel Taplin, Naoya Shibata, Matthew Weyland, and Scott Findlay. “Low magnification differential phase contrast imaging of electric fields in crystals with fine electron probes”. In: *Ultramicroscopy* 169 (2016). Publisher: Ultramicroscopy. DOI: 10.1016/j.ultramic.2016.07.010.
- [57] Zhongbo Li, Johannes Biskupek, Ute Kaiser, and Harald Rose. “Integrated Differential Phase Contrast (IDPC)-STEM Utilizing a Multi-Sector Detector for Imaging Thick Samples”. In: *Microscopy and Microanalysis* 28.3 (2022), pp. 611–621. DOI: 10.1017/S1431927622000289.
- [58] Sihan Wang, Tim B. Eldred, Jacob G. Smith, and Wenpei Gao. “AutoDisk: Automated diffraction processing and strain mapping in 4D-STEM”. In: *Ultramicroscopy* 236 (2022), p. 113513. DOI: 10.1016/j.ultramic.2022.113513.
- [59] James M. LeBeau, Scott D. Findlay, Leslie J. Allen, and Susanne Stemmer. “Position averaged convergent beam electron diffraction: Theory and applications”. In: *Ultramicroscopy* 110.2 (2010), pp. 118–125. DOI: 10.1016/j.ultramic.2009.10.001.
- [60] Jinwoo Hwang, Jack Y. Zhang, Junwoo Son, and Susanne Stemmer. “Nanoscale quantification of octahedral tilts in perovskite films”. In: *Applied Physics Letters* 100.19 (2012), p. 191909. DOI: 10.1063/1.4714734.
- [61] Edgar F. Rauch et al. “Automated nanocrystal orientation and phase mapping in the transmission electron microscope on the basis of precession electron diffraction”. In: *Zeitschrift für Kristallographie* 225.2 (2010), pp. 103–109. DOI: 10.1524/zkri.2010.1205.
- [62] P. A. Midgley and A. S. Eggeman. “Precession electron diffraction – a topical review”. In: *IUCrJ* 2.1 (2015). Publisher: International Union of Crystallography, pp. 126–136. DOI: 10.1107/S2052252514022283.
- [63] Jiwon Jeong, Niels Cauteraerts, Gerhard Dehm, and Christian H Liebscher. “Automated Crystal Orientation Mapping by Precession Electron Diffraction-Assisted Four-Dimensional Scanning Transmission Electron Microscopy Using a Scintillator-Based CMOS Detector”. In: *Microscopy and Microanalysis* 27.5 (2021), pp. 1102–1112. DOI: 10.1017/S1431927621012538.
- [64] Xuhao Hong et al. “Multibeam Electron Diffraction”. In: *Microscopy and Microanalysis* 27.1 (2021), pp. 129–139. DOI: 10.1017/S1431927620024770.
- [65] Steven E Zeltmann et al. “Patterned probes for high precision 4D-STEM bragg measurements”. In: *Ultramicroscopy* 209 (2020), p. 112890. DOI: 10.1016/j.ultramic.2019.112890.
- [66] Ian MacLaren et al. “On the origin of differential phase contrast at a locally charged and globally charge-compensated domain boundary in a polar-ordered material”. In: *Ultramicroscopy* 154 (2015), pp. 57–63. DOI: 10.1016/j.ultramic.2015.03.016.
- [67] Julius Bürger, Thomas Riedl, and Jörg K. N. Lindner. “Influence of lens aberrations, specimen thickness and tilt on differential phase contrast STEM images”. In: *Ultramicroscopy* 219 (2020), p. 113118. DOI: 10.1016/j.ultramic.2020.113118.
- [68] Knut Müller et al. “Atomic electric fields revealed by a quantum mechanical approach to electron picodiffraction”. In: *Nature Communications* 5 (2014), p. 5653. DOI: 10.1038/ncomms6653.
- [69] S. Majert and H. Kohl. “High-resolution STEM imaging with a quadrant detector—Conditions for differential phase contrast microscopy in the weak phase object approximation”. In: *Ultramicroscopy* 148 (2015), pp. 81–86. DOI: 10.1016/j.ultramic.2014.09.009.
- [70] Shahar Seifer, Lothar Houben, and Michael Elbaum. “Flexible STEM with Simultaneous Phase and Depth Contrast”. In: *Microscopy and Microanalysis* 27.6 (2021), pp. 1476–1487. DOI: 10.1017/S1431927621012861.
- [71] Helmut Kohl and Alex Oster. “Optimized detector configurations for the reconstruction of phase-contrast images in scanning transmission electron microscopy”. In: *Ultramicroscopy* (2023), p. 113670. DOI: 10.1016/j.ultramic.2022.113670.
- [72] Biying Song et al. “Hollow Electron Ptychographic Diffractive Imaging”. In: *Physical Review Letters* 121.14 (2018). Publisher: American Physical Society, p. 146101. DOI: 10.1103/PhysRevLett.121.146101.

- [73] Jiamei Song et al. “Atomic Resolution Defocused Electron Ptychography at Low Dose with a Fast, Direct Electron Detector”. In: *Scientific Reports* 9.1 (2019). Publisher: Nature Publishing Group, p. 3919. DOI: 10.1038/s41598-019-40413-z.
- [74] Guanxing Li, Hui Zhang, and Yu Han. “4D-STEM Ptychography for Electron-Beam-Sensitive Materials”. In: *ACS Central Science* 8.12 (2022). Publisher: American Chemical Society, pp. 1579–1588. DOI: 10.1021/acscentsci.2c01137.
- [75] A. M. Maiden, M. J. Humphry, and J. M. Rodenburg. “Ptychographic transmission microscopy in three dimensions using a multi-slice approach”. In: *JOSA A* 29.8 (2012). Publisher: Optica Publishing Group, pp. 1606–1614. DOI: 10.1364/JOSAA.29.001606.
- [76] Georgios Varnavides et al. “Simultaneous Electrostatic and Magnetic Vector Potential Phase Retrieval Using Electron Ptychography”. In: *Microscopy and Microanalysis* 29 (Supplement.1 2023), pp. 278–279. DOI: 10.1093/micmic/ozad067.128.
- [77] Stephanie M. Ribet et al. “Uncovering the three-dimensional structure of upconverting core-shell nanoparticles with multislice electron ptychography”. In: *Applied Physics Letters* 124.24 (2024), p. 240601. DOI: 10.1063/5.0206814.
- [78] Colum M. O’Leary et al. “Three-dimensional structure of buried heterointerfaces revealed by multislice ptychography”. In: *Physical Review Applied* 22.1 (2024), p. 014016. DOI: 10.1103/PhysRevApplied.22.014016.
- [79] K E MacArthur, L B Jones, and P D Nellist. “How flat is your detector? Non-uniform annular detector sensitivity in STEM quantification”. In: *Journal of Physics: Conference Series* 522 (2014), p. 012018. DOI: 10.1088/1742-6596/522/1/012018.
- [80] Taichi Kusumi et al. “New Poisson denoising method for pulse-count STEM imaging”. In: *Ultramicroscopy* (2024), p. 113996. DOI: 10.1016/j.ultramic.2024.113996.
- [81] Ryo Ishikawa et al. “Atomic-Resolution Topographic Imaging of Crystal Surfaces”. In: *ACS Nano* 15.5 (2021). Publisher: American Chemical Society, pp. 9186–9193. DOI: 10.1021/acsnano.1c02907.
- [82] Lewys Jones et al. “Optimising multi-frame ADF-STEM for high-precision atomic-resolution strain mapping”. In: *Ultramicroscopy* 179 (2017), pp. 57–62. DOI: 10.1016/j.ultramic.2017.04.007.
- [83] Emrah Yücelen, Ivan Lazić, and Eric G. T. Bosch. “Phase contrast scanning transmission electron microscopy imaging of light and heavy atoms at the limit of contrast and resolution”. In: *Scientific Reports* 8.1 (2018), p. 2676. DOI: 10.1038/s41598-018-20377-2.
- [84] Ivan Lazić et al. “Single-particle cryo-EM structures from iDPC-STEM at near-atomic resolution”. In: *Nature Methods* 19.9 (2022). Publisher: Nature Publishing Group, pp. 1126–1136. DOI: 10.1038/s41592-022-01586-0.

Supplementary Information

S1 4D-STEM detectors

Summarised in Table S1 are numbers representing the dynamic ranges of the commercially available 4D-STEM detectors displayed in Figure 1 of the paper. While it is inadvisable to compare the dynamic range of detectors directly using either of the given numbers, they are important to take into account because certain experiments may require data with a higher dynamic range. The bit depth gives information about how many bits is used to read out from the detector the information contained in each frame. Note that bit depth does not necessarily tell the full story of the dynamic range of a detector since bits may be used to store other information than the intensity values directly. Additionally, Table S1 gives the highest beam current a detector can withstand without saturating in electrons per pixel per second. This is a physical property of the detector, however it can not be used to compare detectors directly because it does not account for their differing number of pixels.

Table S1: Detector types and dynamic range, given in bit depth and maximum incident beam current before saturation in $e^-/\text{pixel/s}$.

Detector	Type	Bit depth	Maximum count rate ($e^-/\text{pixel/s}$)
EMPAD	PAD	30	$1.2 \cdot 10^7$
EMPAD2	PAD	32	10^9
Arina	PAD	8-32 ¹	10^8
Ela	PAD	8-16 ²	$6.2 \cdot 10^6$
UltraScan	CCD	16	-
Orius	CCD	14	-
OneView	MAPS	12	$2.25 \cdot 10^5$
Rio	Scintillator CMOS	12	$6 \cdot 10^5$
K2	MAPS	32	10*
K3	MAPS	32 ³	40*
Metro	MAPS	32	80*
ClearView	MAPS	12	$3 \cdot 10^6$
Medipix 1	PAD	15	-
MerlinEM	PAD	1-24 ⁴	10^6
Medipix 4	PAD	1-24	-
pnCCD	CCD	16	$4 \cdot 10^5$
Celeritas	MAPS	-	$8.7 \cdot 10^5$
DE-16	MAPS	-	10^5

* Recommended maximum dose rate to ensure detector linearity.

¹8-32 image bit depth, 12 read-out bit depth.

²Speed given in the plot for the Dectris Ela is for the 8 bit read-out.

³The K3 reads out at 32 bit in linear accumulation mode, and 8 bit in counting mode.

⁴For the Medipix/MerlinEM detectors that support a large range of bit depths the speed given in the plot is for 12 bit, but the acquisition speed may be increased by using a lower bit depth.

S2 COM with varying detector geometries

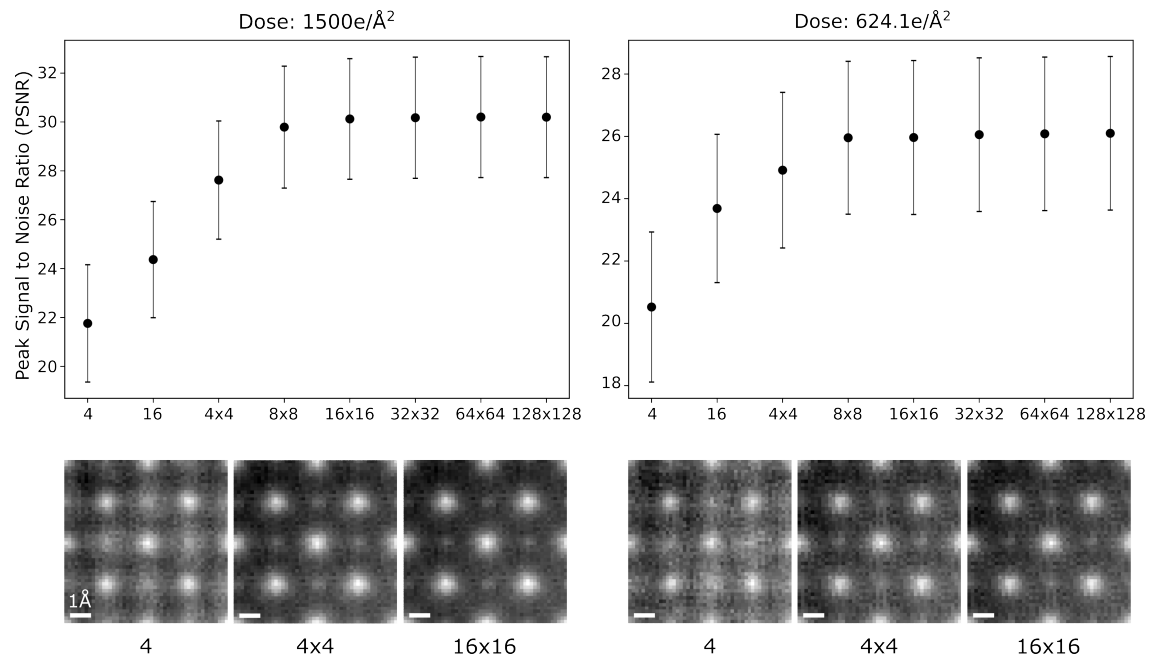


Figure S1: Peak Signal to Noise Ratio (PSNR) in simulated finite dose iCOM images. Cut-out of the top left corner of the reconstructed images for detector geometries annular four-segmented, 4x4 pixel array, and 16x16 pixel array are shown beneath.

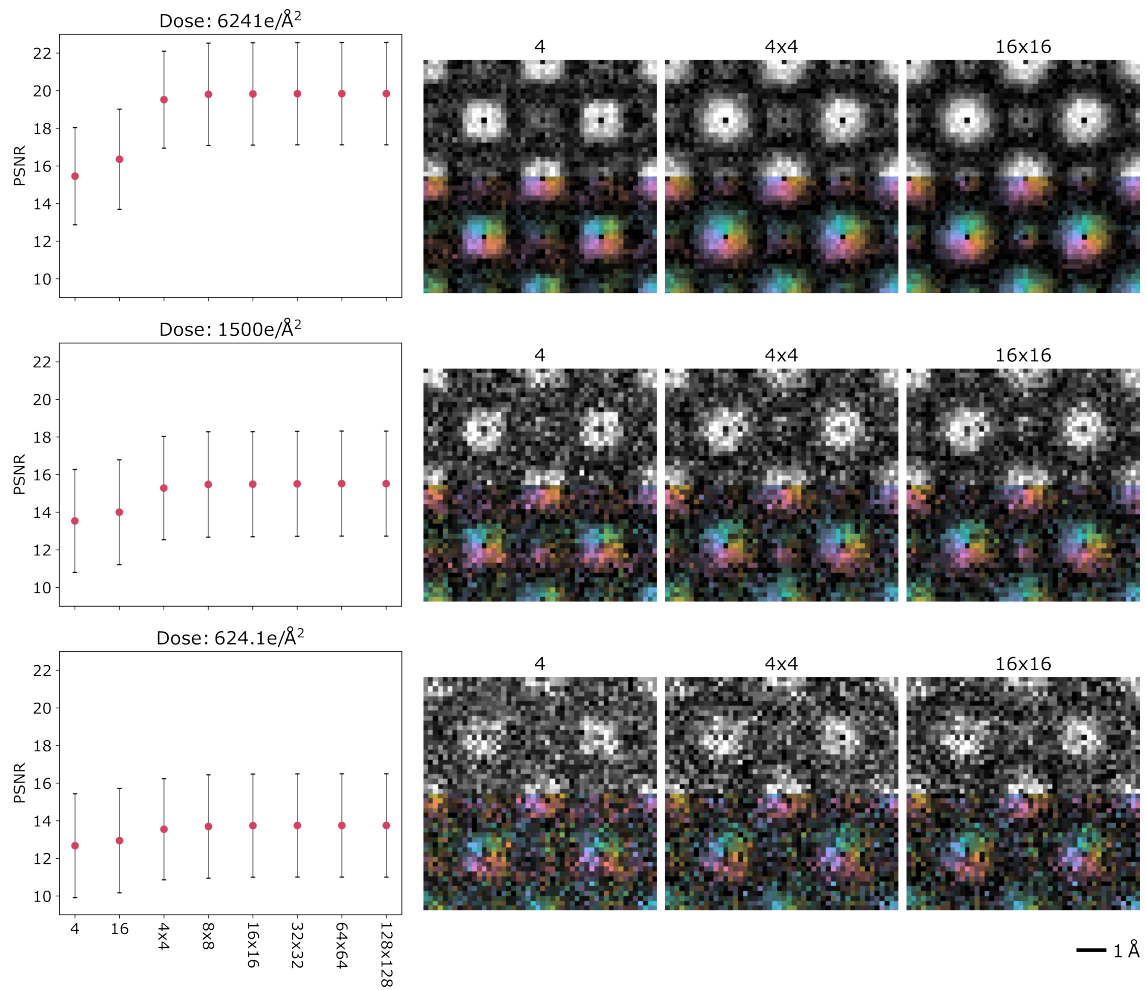


Figure S2: PSNR in simulated $|\text{COM}|$ images for finite doses 6241, 1500, and $624.1 e/\text{\AA}^2$, plotted with the same y-axis in order to clearly show how the PSNR goes down with decreasing dose. The reference image is the infinite dose $|\text{COM}|$ image as calculated from the full 4D-STEM

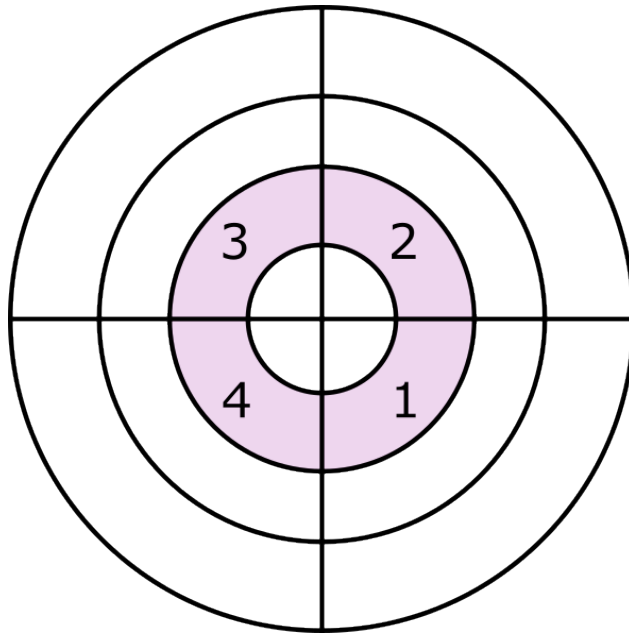


Figure S3: Illustration of the geometry of the segmented annular all field (SAAF) detector. The second ring (highlighted) was used for both the analog and digitised imaging in this study.

S3 Experimental digitisation

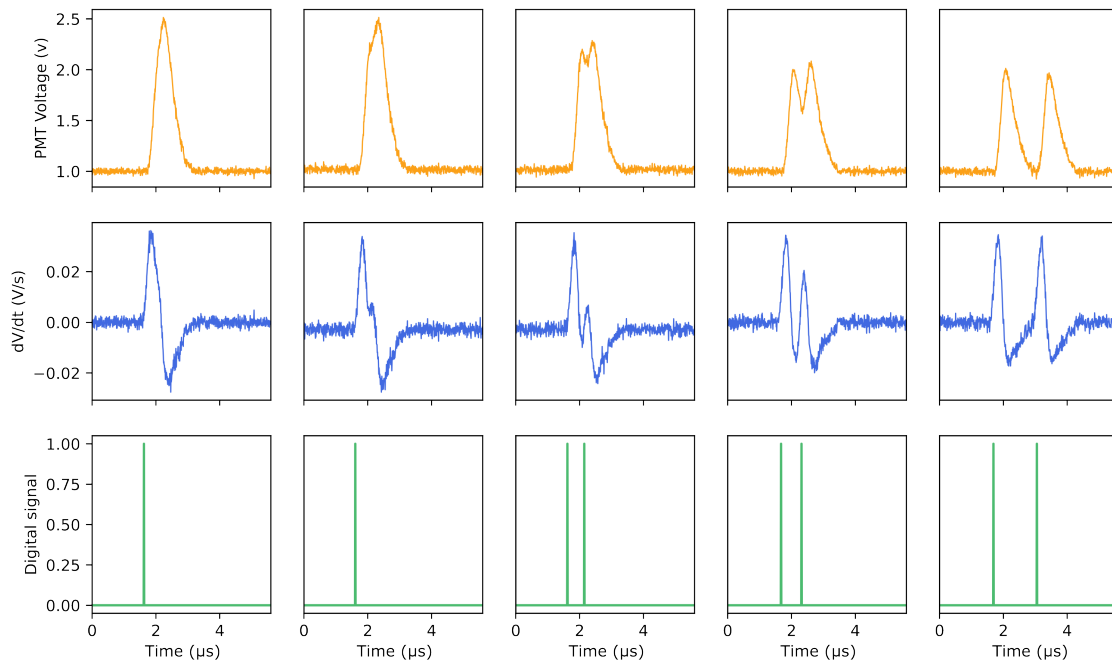


Figure S4: Illustration of electron detection events with increasing separation in time eventually allowing them to be digitised as two separate events. The statistically acceptable separation time for two events to be separated was determined by simulating two events at increasing separation and recording when they were detected as two digitised events. The average separation of 259 ± 26 ns was obtained from 200 such simulations.

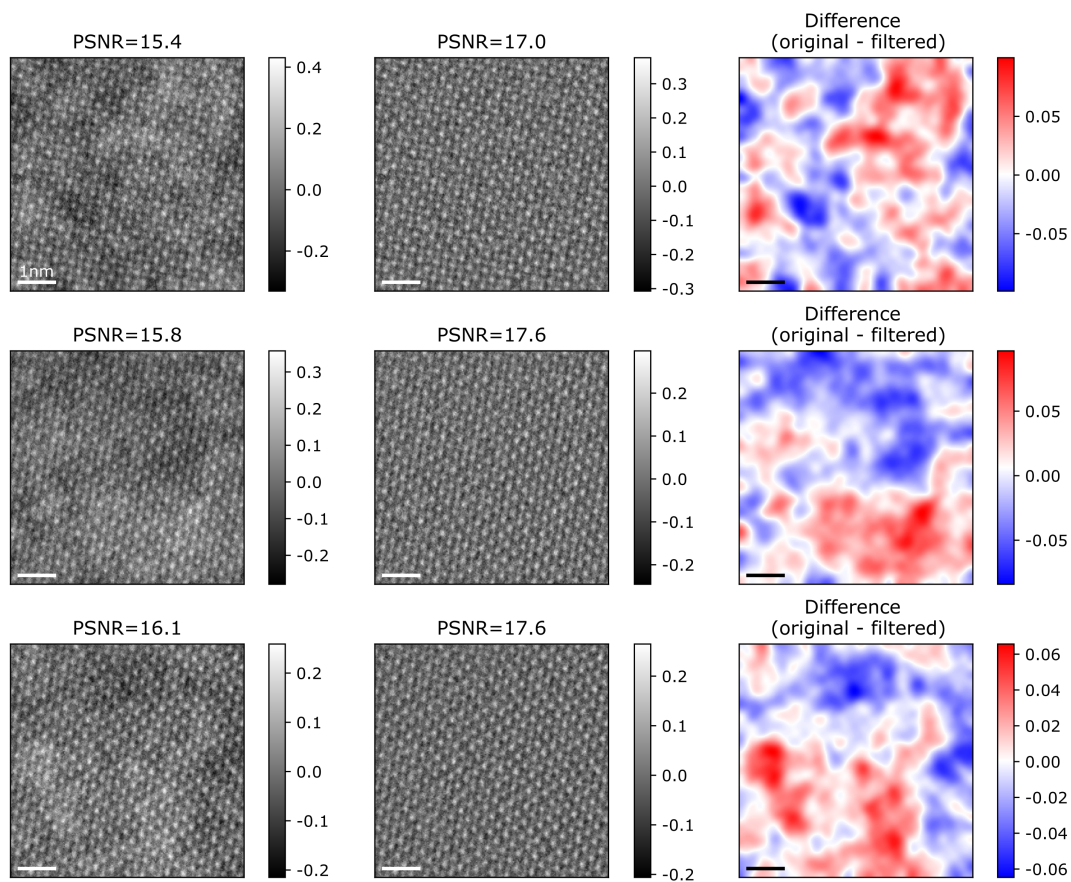


Figure S5: Unfiltered and high-pass filtered experimental images and their difference. The high-pass filtered image was computed by subtracting a low-pass filtered version of the unfiltered image (Gaussian blur with $\sigma = 10$).

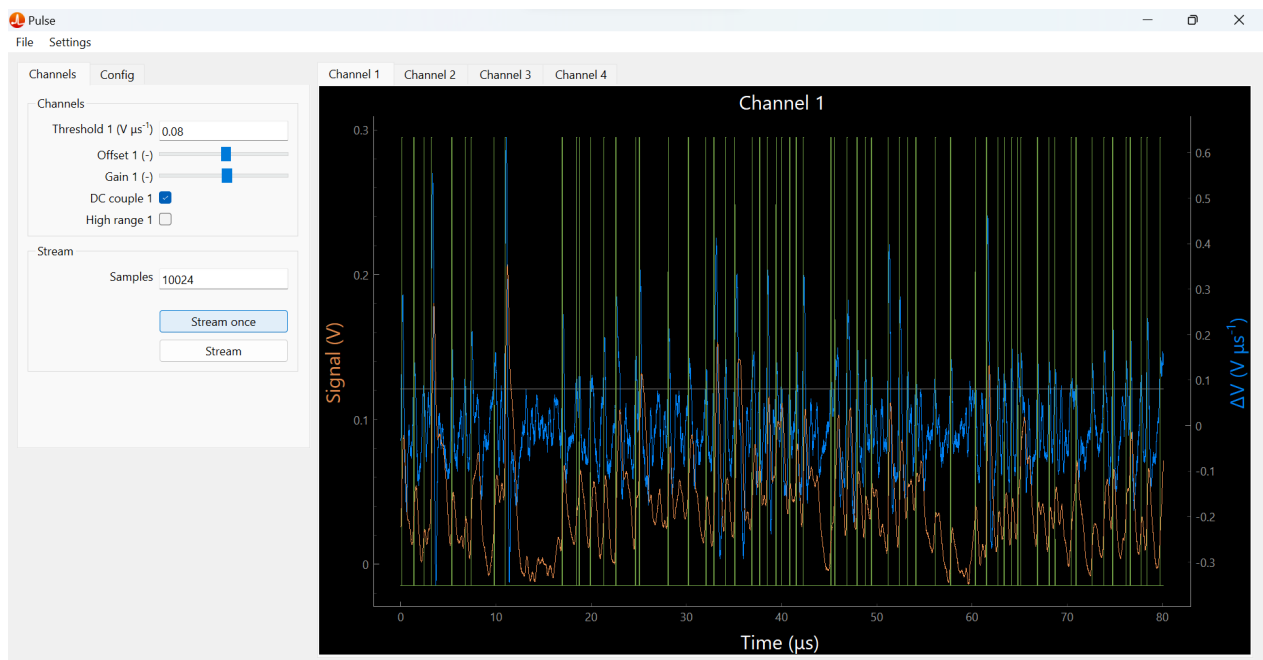


Figure S6: Screenshot of the software controlling the Pulse digitiser unit. The display shows the raw data stream (in orange), the gradient (in blue), the threshold (horizontal gray line), and the digitised events (in green) for Channel 1. The sidebar shows the settings for this channel.